Computational characterization of millimetre-wave heat exchangers with an AlN:Mo susceptor of multiple cylindrical elements

Catherine M. Hogan, Brad W. Hoff, Ian M. Rittersdorf & Vadim V. Yakovlev

Taylor & Francis
Taylor & Francis Group

Check for updates

RESEARCH ARTICLE

Computational characterization of millimetre-wave heat exchangers with an AlN:Mo susceptor of multiple cylindrical elements

Catherine M. Hogan[a], Brad W. Hoff[b†] (iD), Ian M. Rittersdorf[c] (iD) and Vadim V. Yakovlev[a] (iD)

[a]Department of Mathematical Sciences, Worcester Polytechnic Institute, Worcester, MA, USA; [b]Air Force Research Laboratory, Albuquerque, NM, USA; [c]Naval Research Laboratory, Washington, DC, USA

ABSTRACT

A concept for a millimetre-wave (MMW) heat exchanger (HX) featuring AlN:Mo ceramic composite structures as electromagnetic absorbing elements (susceptors) has been recently introduced as a receiving device in power beaming applications. Earlier computational studies of electromagnetic and thermal processes have shown reasonable energy efficiency and exceptional uniformity of MMW-induced temperature fields in a single cubic susceptor with concentration of Mo doping on the level of 3–4% by volume. As part of ongoing research, a MMW HX comprised of an array of cylindrical susceptors is proposed to potentially enable increased robustness against thermal stress and reduced manufacturing cost. In this paper, we computationally study the effects driven by such a change and demonstrate feasibility of the designs based on multiple cylinders. We present the output of electromagnetic and coupled electromagnetic-thermal simulations of a prospective physical prototype of a HX with five cylinders on a square metal base plate. Three alternative layouts with four, nine, and sixteen cylindrical elements that are suggested by the highest density packing of equal circles in a square are also analyzed. It is shown that, in comparison with the previously studied case of a single cubic susceptor, energy efficiency of all systems with Mo = 3–4% is down from 50–55% to 35–45%. While temperature distribution within each individual cylinder remains highly uniform, maximum temperatures of different cylinders may be different by up to 30–40 °C; when the angle of incidence deviates from normal, this difference further increases: e.g. when the angle is 10°, in the sixteen-cylinder system, it may reach 120–130 °C.

1. Introduction

Beyond the traditional application areas of electromagnetic (EM) heating, such as food engineering, chemistry and materials science, this technology is being evaluated for

CONTACT Vadim V. Yakovlev ✉ vadim@wpi.edu 🖃 Department of Mathematical Sciences, Worcester Polytechnic Institute, Worcester, MA 01609, USA.

potential utility in power beaming applications (Koert and Cha 1992; Jamnejad and Silva 2008; Sayigh 2012; Rodenbeck et al. 2021). The EM heat exchangers (HX) are used in thermal thrusters employing EM energy to produce thrust by thermal expansion of a compressed gas (Parkin, DiDomenico, and Culick 2004), beamed energy propulsion (Landis 1999; Coopersmith and Davis 2016), solar thermal collectors (Jamar et al. 2016), and wireless energy transfer (Brown and Eves 1992; Benford 2008; Mohekar et al. 2018; Mohekar, Tilley, and Yakovlev 2019a; Mohekar, Tilley, and Yakovlev 2019b).

A new EM HX configuration has been recently introduced for ground-to-ground millimetre-wave (MMW) power beaming applications (Jawdat et al. 2017; Hoff et al. 2018; Kumi et al. 2020a; Kumi et al. 2020b). Conceptually, it is comprised of an array of ceramic tile-like elements affixed to a metal baseplate that contains channels with fluid flow. The EM power of the incident wave is dissipated in the bulk of the ceramic elements, generating heat, and this heat is conducted from the ceramic tiles to the attached baseplate with the fluid flowing along the channels and taking the heat away. Theoretical studies behind this concept show a potential for high efficiency of layered structures due to a possible resonance-based control over thermal runaway (Mohekar, Tilley, and Yakovlev 2019b; Gaone, Tilley, and Yakovlev 2019; Mohekar, Tilley, and Yakovlev 2020). A computer model of a MMW HX with a susceptor made as a single rectangular block of a ceramic composite (aluminium nitride doped with molybdenum, AlN:Mo) (Kumi et al. 2020a, 2020b) have shown elevated energy efficiency and high level of uniformity of the MMW-induced temperature field. However, while these results further stimulated the development of the technology, the cost-effective production of mechanically robust AlN:Mo elements and practicality of exploitation of the device suggest that the physical prototype of the MMW HX to use multiple cylindrical susceptors. In this case, the pieces of the absorbing ceramic element become separated by air gaps and a substantial part of the metal baseplate is exposed to the incoming EM field. An extent of inevitable changes in characteristics of the MMW HX is therefore of significant interest.

In this paper, we present computational results demonstrating feasibility of the design of the prospective physical prototype that features five AlN:Mo cylinders on a square metal plate. We also study three alternative layouts of the cylinders that are suggested by the highest density packing of equal circles in a square (Goldberg 1970; Boll et al. 2000; Maranas, Floudas, and Pardalos 1995) and possess four, nine, and sixteen elements. We show that energy efficiency of all fours systems is an increasing function of concentration of molybdenum doping in the composite and reaches its highest values for Mo = 3–4% by volume; however, it is lower than in the case of a single cubic susceptor. Uniformity of temperature distribution within individual cylinders is always very high, but in the systems with higher numbers of cylinders the maximum temperatures of different cylinders may differ by 30–40 °C. It is also shown that, despite the increased absorbing surface area in four-, nine- and sixteen-cylinder systems, their energy efficiency is about the same as in the five-cylinder system. In case of off-normal incidence, the surface area exposed to the MMW is further increased, but energy efficiency remains to be about the same; however, the difference between temperatures of different cylinders is notably larger: for example, in the sixteen-cylinder system, it may be above 100 °C.
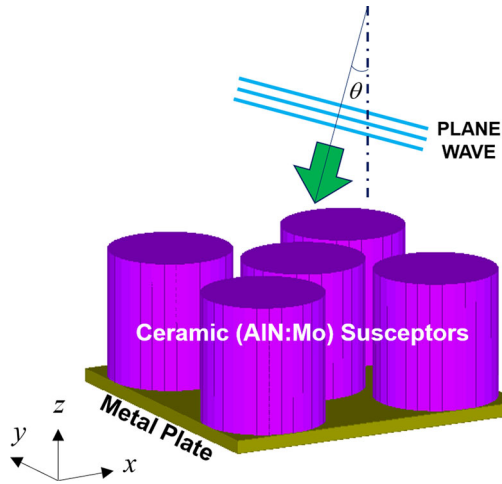
Figure 1. Model of the MMW HX physical prototype: five cylinders on a metal plate; normal or off-normal plane wave incidence from the top.

2. Methodology

Computational experiments were conducted based on simulation of the EM and thermal phenomena occurring in the HX with AlN:Mo cylindrical susceptors irradiated by high-power MMW. The simulations were carried out with the 3 D conformal finite-difference time-domain (FDTD) technique implemented in *QuickWave*[TM] (QuickWave 1998–2020). The models employed in the present study were built as modifications of the EM-thermal model (Kumi et al. 2020b) for a rectangular AlN:Mo block on a metal plate. That model was verified against the model of the same system built in *COMSOL Multiphysics*[TM] (COMSOL Multiphysics 1998–2020).

The first model reproduces the prospective physical prototype which consists of an array of five cylindrical susceptors standing on a thin metal plate and irradiated by a plane wave, as shown in Figure 1. The layout specified in Figure 2 features an air gap between the points of cylinders' contacts that is required to accommodate thermal expansion of the ceramic material.

Temperature-dependent EM and thermal parameters of AlN:Mo are assembled in (Kumi et al. 2020b) as generalization and adaptation of experimental data (Hilario et al. 2017; Hilario et al. 2019; Hoff et al. 2019a; Hoff et al. 2019b). Data on the composites with six different Mo concentrations, ranging from 0.25% to 4.0% (by volume), includes dielectric constant (ε') and the loss factor (ε'') (at 95 GHz) as well as specific heat (c_p) and thermal conductivity (k) in the interval from 20 to 1,000 °C. While dielectric properties are characterized by a slow linear growth with temperature, the decrease of the thermal parameters is substantial and well approximated by polynomials of order 3 and 4. Values of density for all six materials were assumed to be temperature independent. Typical data on all material parameters is exemplified in Table 1.

In the coupled simulation, the EM and thermal FDTD solvers operate as parts of an iterative procedure (Kopyt and Celuch 2007; Celuch and Kopyt 2009; Koutchma and Yakovlev 2010; Yakovlev et al. 2011) in which a steady state solution of the EM
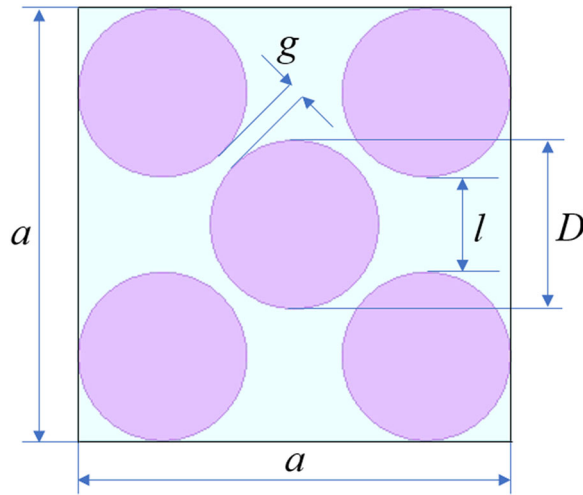
Figure 2. Cross-sectional geometry of the physical prototype: $a = 24.4$ mm, $D = 9.5$ mm, $l = 5.4$ mm, $g = 1.0$ mm.

Table 1. Dielectric (at 95 GHz) and thermal properties of AlN:Mo composite at the endpoints of the operating temperature interval (Adapted from (Kumi et al. 2020b)).

Mo (%)	Temperature (°C)	Dielectric constant (ε')	Loss factor(ε'')	Density (ρ) (g/cm^3)	Specific heat (c_p) (J/gC)	Thermal conductivity (k) (W/cmC)
0.25	20	8.61	0.029	3.32	0.702	1.403
	1,000	9.40	0.068		1.142	0.385
0.5	20	8.76	0.036	3.33	0.704	1.242
	1,000	9.54	0.085		1.142	0.425
1.0	20	9.09	0.050	3.37	0.692	1.300
	1,000	9.88	0.099		1.136	0.390
2.0	20	9.96	0.120	3.44	0.681	1.375
	1,000	10.94	0.198		1.129	0.349
3.0	20	11.48	0.465	3.50	0.668	1.374
	1,000	12.66	0.661		1.123	0.359
4.0	20	13.45	1.167	3.57	0.658	1.345
	1,000	14.73	1.559		1.124	0.362

problem becomes an input for the thermal problem. The heating occurs for the time specified in the preset heating time step Δt, after which the process returns to the EM solver. In all subsequent runs of the EM solver, material parameters are upgraded in every cell of the applied FDTD mesh in accordance with the temperature field outputted from the thermal solver. The latter determines temperature field established in the absorbing material after each Δt; after a certain number of iterations, maximum temperature of the process (not exceeding the maximum value in the data on temperature-dependent material parameters) is reached, and the solution process stops.

In the implementation of the open scenario in a finite-size FDTD model, the system with the cross-section in Figure 2 (with the height of the AlN:Mo cylinders 10 mm and the thickness of the metal plate 1 mm) is surrounded by the 28×28 x 18 mm plane wave box with the 28×28 mm face on the top responsible for excitation of the incident plane wave. This box, in its turn, is situated inside the 34×34 x

24 mm rectangular space whose boundaries imitate the Mur superabsorbing boundary condition (QuickWave 1998–2020).

Following the steps in (Kumi et al. 2020b), to satisfy the FDTD stability criterion and minimize computational recourses, the model of a MMW HX irradiated by the plane wave with the wavelength of 3.17 mm is discretized with the mesh with maximum cell sizes of 0.29 mm (in air) and from 0.075 to 0.095 mm (in the ceramic composite, in accordance with dielectric constants ε' related to Mo = 4% ($\varepsilon' = 14.73$) and 0.25%, ($\varepsilon' = 9.54$) and the highest temperature of 1,000 °C, respectively). Therefore, depending on the Mo content, the model of the 5-cylinder system comprises 15.3 to 27.3 million cells (1.456 and 2.603 MB RAM, respectively).

To characterize energy efficiency of the MMW heating process, following (Kumi et al. 2020b), we calculate the parameter $\eta = P_d/P$, where P_d is density of the power dissipated in the composite susceptors and P is the power density of the incident plane wave. Values of P_d are computed by the EM model for different concentrations of Mo in the ceramic composite and its temperatures, and temperature is introduced in EM simulation through the values of complex permittivity $\varepsilon = \varepsilon' - i\varepsilon''$ (with dielectric constants ε' and the loss factor ε'') at particular temperatures.

As power densities, P_d and P relate to the total area of the absorbing surfaces of the cylindrical susceptors and the area of the square metal plate carrying all the cylinders, respectively. In case of a normal incidence, the absorbing surface consists of the circular areas on the top of the cylinders, whereas in case of off normal deviation of the incident wave it also includes the projections of the side cylindrical surfaces exposed to the EM field onto the plane perpendicular to the direction of wave propagation.

The thermal problem is solved on the same mesh as the EM problem under Neumann (adiabatic) boundary conditions on all (ceramic-air and ceramic-metal) interfaces.

In this paper, we present simulations performed on a Window 10 workstation with two Intel Xeon Gold 5120 processors with a base/peak frequency of 2.2/3.2 GHz (each having 14 cores and supporting 28 threads), the GPU NVIDIA Quadro P5000 and 1 TB RAM.

The design in Figure 1 is characterized by the ratio of the absorbing ceramic surface to the reflecting surface of the square metal plate being $d = 0.598$, and this implies that this layout may be responsible for lower energy efficiency than a single square susceptor (Kumi et al. 2020b; Rittersdorf et al. 2021) with $d = 1$. The solution of the problem on the packing of equal circles in a square (Goldberg 1970; Boll et al. 2000; Maranas, Floudas, and Pardalos 1995) provides the highest value of d (0.785) for four, nine, and sixteen cylinders arranged in rigorous rows and columns. This suggests feasibility of studying the layouts of the cylindrical susceptors shown in Figure 3 as possible alternative designs.

Similar models reproducing the cylinders' layout of these three configurations (for the same $a = 24.4$ mm) were developed and used for a comparative computational analysis. These models are different only in geometry of the susceptors (and are thus of about the same size), so their details are omitted here.
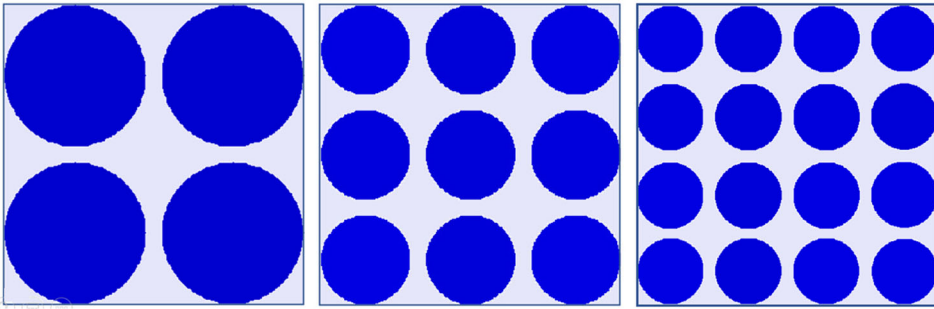
Figure 3. Layouts of ceramic cylinders in the packings of equal *n* circles in a square for $n = 4$ (a), $n = 9$ (b), and $n = 16$ (c) with 1 mm gap between the contact points.

3. Computational results

3.1. Normal incidence

Simulation of EM processes in the five-cylinder system displays the highest energy efficiency when the cylinders are made of the composite with 3.0–4.0% Mo (Figure 4(a)). This is consistent with the results for the system with a single rectangular block (Kumi et al. 2020b) (red dots in Figure 4(a)), though here the efficiency is down from 53–55 to 37%. We explain this drop by the decrease of the surface area of the susceptors exposed to the plane wave.

Average values of η of the four-, nine-, and sixteen-cylinder systems also grow with concentration of Mo, and, in accordance with an expectation of higher efficiency of the systems with higher *d*, they reach slightly higher levels − 40 to 46% for Mo = 3–4%. This makes the composites with that level of Mo doping preferential (in terms of energy efficiency) for MMW HX of all considered designs. This is also consistent with the results (represented here by a red curve in Figure 4(a)) for the single cubic susceptor (Kumi et al. 2020b).

The EM simulation allows us to visualize the electric field in and around the absorbing cylinders and, in particular, compare it for different Mo contents. Growth of molybdenum concentration from 0.25 to 4% corresponds to the 1.5 times increase of dielectric constant and the drastic (nearly 30 times) jump up of the lost factor (see Table 1). Penetration of the field in the composite with higher contents of Mo is, therefore, much lower, and Figure 5 shows that the magnitude of the electric field in air between and around the cylinders is much higher in case of Mo = 3% than 0.25%. For all Mo contents, formation of standing wave in the space between the cylinders is also apparent whereas the field is more uniform within the cylinders with higher concentration of Mo (and thus higher loss factor).

Another valuable output of the EM simulation is patterns of dissipated power induced within the absorbing materials by the incident plane MMW. Computed for the five-cylinder system with the susceptors of different concentration of Mo, those patterns were found to be characterized by large amounts of local maxima (hot spots). The amount and magnitudes of those maxima spread over all the cylinders, and this suggest that, because of the high thermal conductivity of the AlN:Mo composites, the material may be heated sufficiently uniformly. The profiles of those patterns are qualitatively completely similar to the patterns in the MMW HX with one
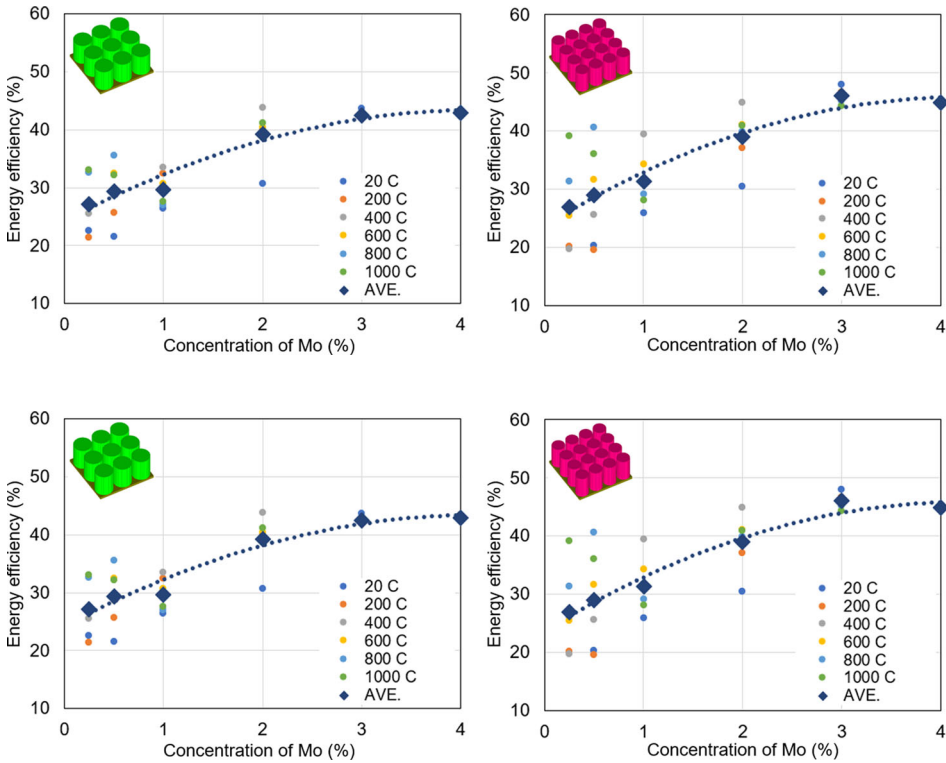
Figure 4. Energy efficiency η (at different temperatures of the AlN:Mo composite and average) of the five-cylinder system (a) and the systems with four (Figure 3(a)) (b), nine (Figure 3(b)) (c), and sixteen (Figure 3(c)) (d) cylinders as functions of contents of Mo; normal incidence ($\theta = 0$); red points in (a) characterize the system with one rectangular cubic susceptor.

single cubic block analyzed in (Kumi et al. 2020a; Kumi et al. 2020b) and, for sake of brevity, are not presented in this paper.

Simulation of the temperature field induced in the ceramic susceptors by the incident plane MMW shows (*i*) the time-temperature heating characteristics and (*ii*) temperature distributions within the absorbing (hence heated) cylinders at different time instances. It is seen from Figure 6 that when the plane wave with incoming power density of 357 W/mm^2 hits the five-cylinder system, then, in the composite with the lowest content of Mo (0.25%), the temperature of 1,000 °C is reached for about 90 s; however, in the system made of AlN:Mo with Mo = 4%, this level is reached for about 50 s. For every concentration, the time characteristics of minimum and maximum temperatures are very close to each other.

The last observation suggests that the temperature distributions within the ceramic absorbers may be highly uniform, and this is confirmed by a series of patterns in Figure 7 that show time evolutions of the temperature field in the susceptors made of six composite materials. The patterns are remarkably uniform for all concentrations. (This, in turn, justifies the assumption about uniformity of heating that was implicitly made in computations of energy efficiency at different temperatures (Figure 8) by the EM model.) High level of uniformity is kept up to the final stage of each heating
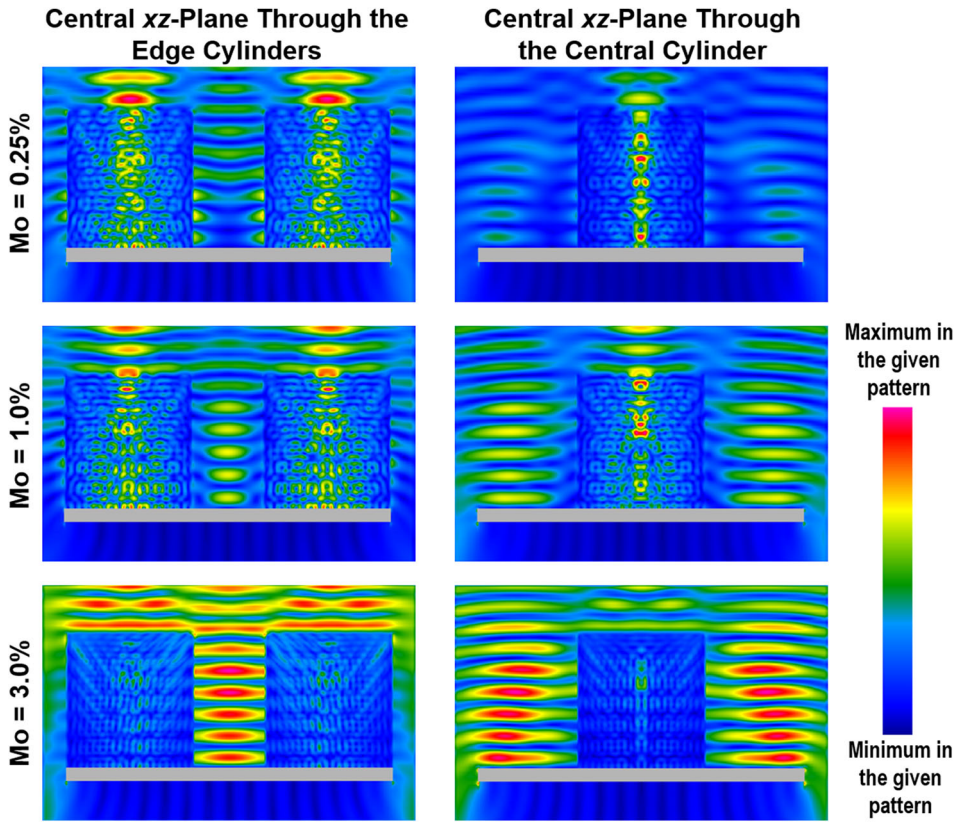
Central *xz*-Plane Through the Edge Cylinders

Central *xz*-Plane Through the Central Cylinder

Mo = 0.25%

Mo = 1.0%

Mo = 3.0%

Maximum in the given pattern

Minimum in the given pattern

Figure 5. Relative patterns of the electric field envelopes in the vertical (xz-) planes through the five-cylinder system for different concentrations of Mo in the ceramic composite susceptors.
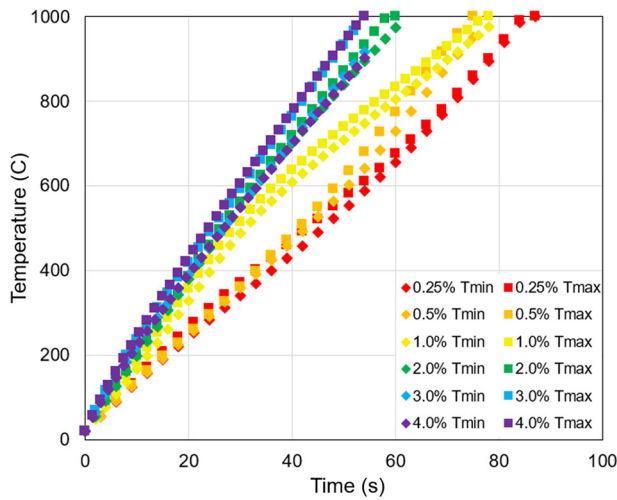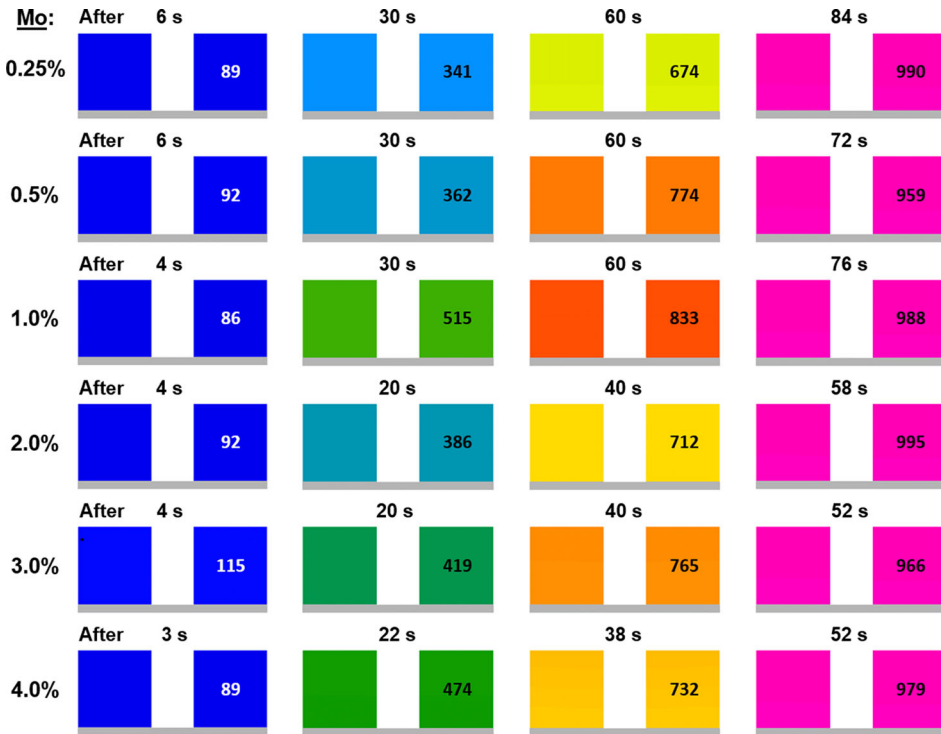
Figure 6. Time characteristics of minimum and maximum temperatures (T_{min} and T_{max}) of the AlN:Mo susceptor of the 5-cylinder experimental system; the absorbing composite with different concentrations of Mo (0.25 to 4%); normal incidence; incoming power density 357 W/mm^2.

Figure 7. Time evolution of the temperature field in the vertical (xz-) plane through the two edge cylinders (a) and in the central horizontal (xy-) plane through the all cylinders (b) with Mo = 0.25, ... , 4.0% in the five-cylinder system; maximum values of temperature are shown on each pattern; patterns are normalized to the minimum and maximum temperatures of the process (Scale A, Figure 8); heating time steps in simulations are 3 (Mo = 0.25 and 0.5%), 2 (Mo = 1.0, 2.0, and 3.0%), and 1.5 s (Mo = 4.0%); incoming power density 357 W/mm^2.

process for each individual cylinder and is maintained for the system of all five cylinders.

Computation of temperature patterns in the four-cylinder system (characterized by higher ratio $d = 0.722$) shows a very similar heating process (Figure 9), but even more consistent temperature distributions: all four cylinders are heated at about the same rate with very similar cross-sectional patterns. Simulation of the heating in the system with higher numbers of cylinders ($n = 9$) (Figure 10) shows that the central cylinder is heated slightly slower such that at the final stage of heating its maximum temperature could be lower by 40–60 °C. On the other hand, the four-cylinder system takes the longest to reach 1,000 °C; yet, the delay is only 10 s in comparison with the nine-cylinder system, which is the fastest.

The chief cause for this uncharacteristically homogeneous temperature distribution generated by EM heating is a high level of thermal conductivity of AlN (Figure 11) (Sienna Technologies 2011; Hoff et al. 2019a) that is maintained with the incremental Mo doping. It is shown in (Kumi et al. 2020b) that in a MMW HX based on a single AlN:Mo block dissipated power patterns characterized by dozens of strong hot spots are converted into highly uniform temperature distributions maintaining their uniformity for the entire times of the heating processes. Here, in the designs based on
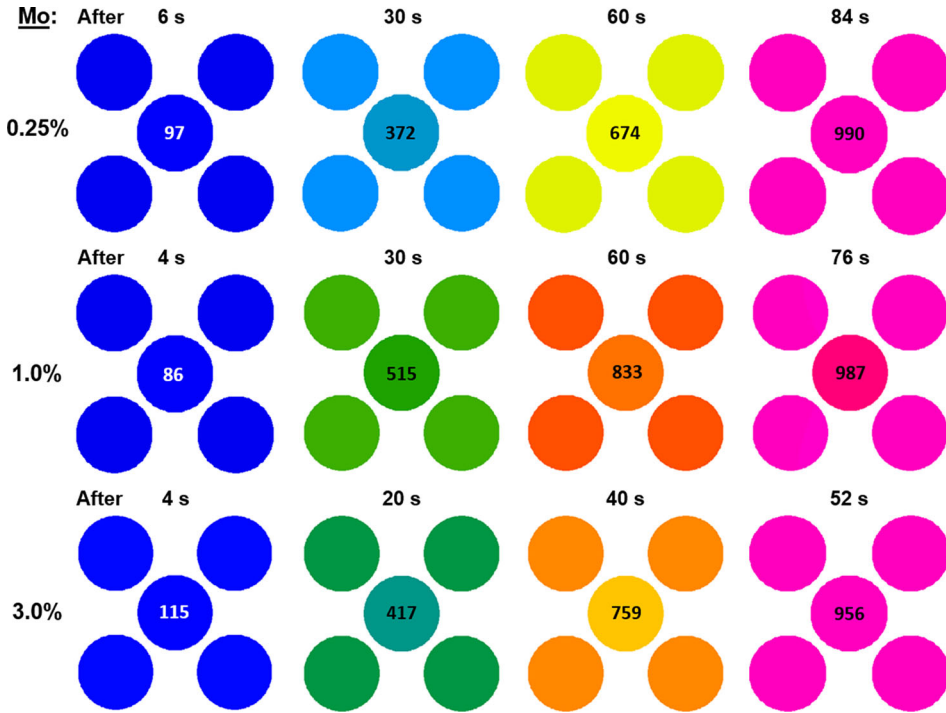
Figure 7. Continued.

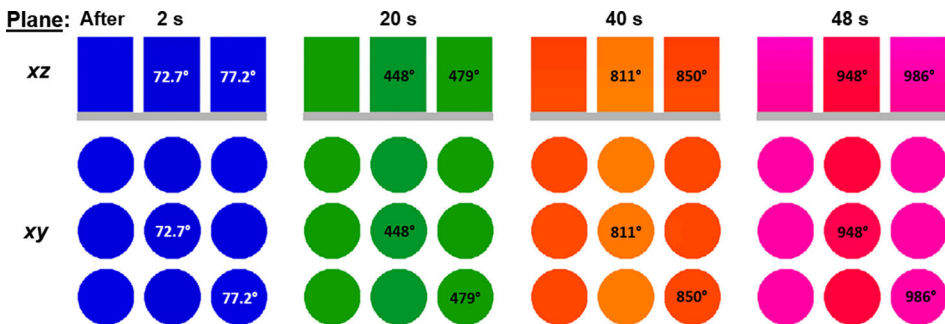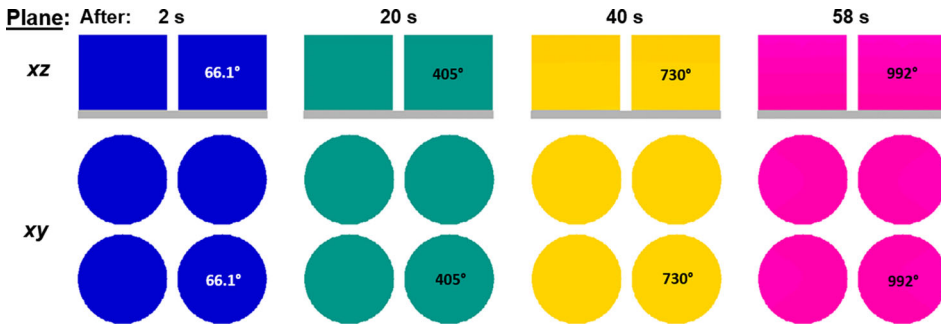**Figure 8.** Scales for normalization of temperature fields.

Figure 9. Time evolution of the temperature field in the vertical (xz -) plane through the two edge cylinders and in the central horizontal (xy-) plane through the all cylinders with Mo = 3.0% in the four-cylinder model; maximum values of temperature are shown on each pattern; patterns are normalized to the minimum and maximum temperatures of the process (Scale Am Figure 8); heating time step in simulation is 2 s; incoming power density 430 W/mm^2.

Figure 10. Time evolution of the temperature field in the vertical (xz -) plane through the three edge cylinders and in the central horizontal (xy-) plane through the all cylinders with Mo = 3.0% in the nine-cylinder model; maximum values of temperature are shown in each pattern; patterns are normalized to the minimum and maximum temperatures of the process (Scale A, Figure 8); heating time step in simulation is 2 s; incoming power density 394 W/mm^2.
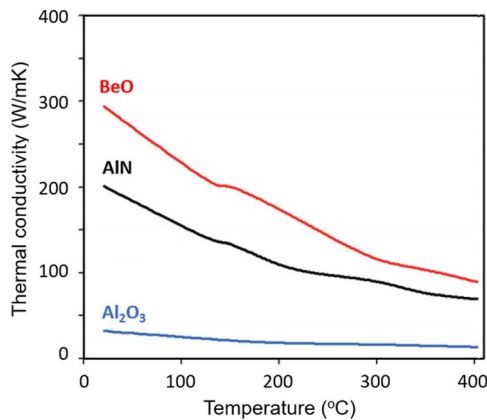

Figure 11. Temperature characteristic of thermal conductivity for three most conductive common ceramics – alumina, aluminium nitride, and beryllium oxide; adapted from (Sienna Technologies 2011).

separately standing cylindrical absorbers, we observe a similar phenomenon for each individual cylinder whereas the temperatures of different elements, especially for higher n, can differ by up to 30–40 °C.

3.2. Off normal incidence

In real-life applications of MMW HXs, deviation of the plane wave from a normal incidence is inevitable. In this case, operational characteristics of the susceptor consisting of multiple cylinders are particularly difficult to predict since the area of absorbing surface is larger than the sum of n circular areas (A_n) and includes portions of the side surfaces of the cylinders. In this section, we present selected computational results for energy efficiency and temperature fields that allow one to assess functionality of MMW HXs with cylindrical susceptors for the angle of incidence θ in the interval $0 < \theta \leq 15°$.
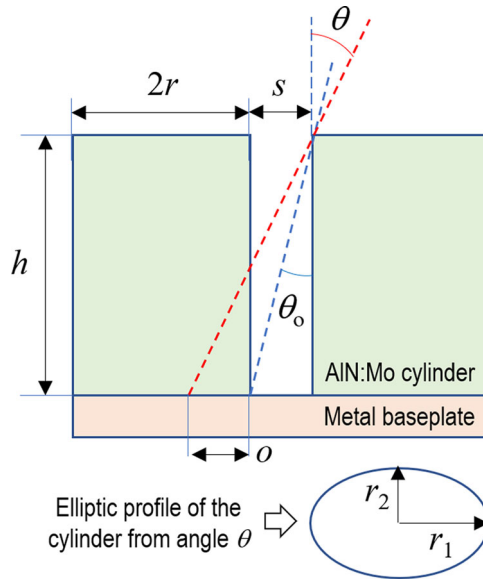
Figure 12. xz-plane geometrical parameters involved in computation of the exposed surface area in case of off-normal incidence.

Since determination of energy efficiency requires data on dissipated power density, knowledge of the surface area of the cylindrical susceptors exposed to the incoming field and seen in the plane perpendicular to the direction of propagation it required. For the models, where the number of cylinders is a perfect square number (i.e. the four-, nine-, and sixteen-cylinder model) this area can be found under the assumption that when a circle of radius r is viewed from an angle $0 \leq \theta < 90°$, the circle becomes an ellipse with semi-major axes $r_1 = r$ and $r_2 = r \cos\theta$ (Figure 12).

There are two scenarios to consider here: when the cylinders do not overlap one another (i.e. when the surface area of a cylinder covers a portion of another cylinder), and when the cylinders do overlap one another. The overlap occurs when $\theta > \tan^{-1}(s/h)$, thus, for all HXs considered in this work, $\theta > \theta_0 = 5.7°$ (Figure 12). If there is no overlap, the total exposed surface area is equal to the exposed surface area of a single cylinder times n. If there is overlap, then this overlapping area must be subtracted from the total surface area.

All in all, the total exposed surface area A_{off} of the multicylinder system with $n = 4$, 9, and 16 in case of off-normal incidence of the plane wave is given by the formula

$$A_{\text{off}} = nA_c - \sqrt{n}(\sqrt{n} - 1)A_0 \tag{1}$$

where

$$A_c = A_e + \frac{1}{2}tc_e,$$

$$A_e = \pi r_1 r_2,$$

$$c_e = 2\pi \sqrt{r_1^2 - \frac{r_1^2}{r_2^2}\left(r_2 - \frac{o}{2}\right)^2},$$

$$A_0 = 2(A_s - A_t),$$

$$A_t = uv,$$

$$u = \pm \sqrt{r_1^2 - \frac{r_1^2}{r_2^2}\left(r_2 - \frac{o}{2}\right)^2}$$

$$v = r_2 - \frac{o}{2}$$

$$A_s = F(\varphi_2) - F(\varphi_1)$$

$$\varphi_{1,2} = \frac{\pi}{2} \mp \frac{\varphi}{2}$$

$$\varphi = 2\tan^{-1}\frac{u}{v}$$

$$F(\varphi) = \frac{r_1 r_2}{2}\left[\varphi - \tan^{-1}\frac{(r_2 - r_2)\sin 2\varphi}{r_1 + r_2 + (r_2 - r_2)\cos 2\varphi}\right]$$

Calculation of the exposed area shows that, as seen in Figure 13, when θ reaches the value of $\theta_0 = 5.7°$, the area is larger than the one in case of a normal incidence by 1.15 to 1.3 (depending on the values of n). Moreover, the ratio A_{off}/A_n grows with the further increase of θ because not only the area of the absorbing surface on the sides of the cylinders becomes larger, but also the reflecting portion of the baseplate are now entirely shadowed. Also, it appears that an oblique incidence does not change the trend of energy efficiency increasing with concentration of Mo (Figure 14). As in case of a normal incidence, for high values of Mo, energy efficiency is practically temperature-independent; when Mo = 3%, it exceeds the efficiency supported by composites with low Mo contents by at least 10–15%.

While these results may imply higher energy efficiencies for larger angles of deviation, this effect, however, is not observed: the graphs in Figure 15 show either 1–2% increase (four and nine cylinders), or 1% decrease (sixteen cylinders) for the composite with Mo = 3%. It appears that multiple factors supporting and preventing the increase of η with the increase of θ (such as decrease of the area of reflecting metal surface, increase of the area of absorbing composite surface, absence or presence of the shadow shed on some cylinders by others, etc.) come to some balance.

Finally, Figures 16 and 17 present the examples of temperature patterns induced in the four- and sixteen-cylinder systems, respectively, by the incoming field deviating
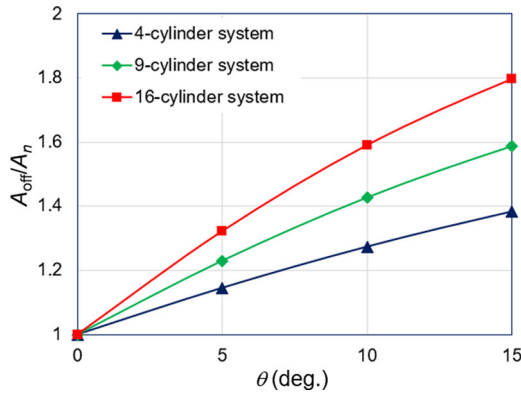
Figure 13. Ratio of the exposed areas (oblique incidence over normal one) as function of angel of deviation θ.
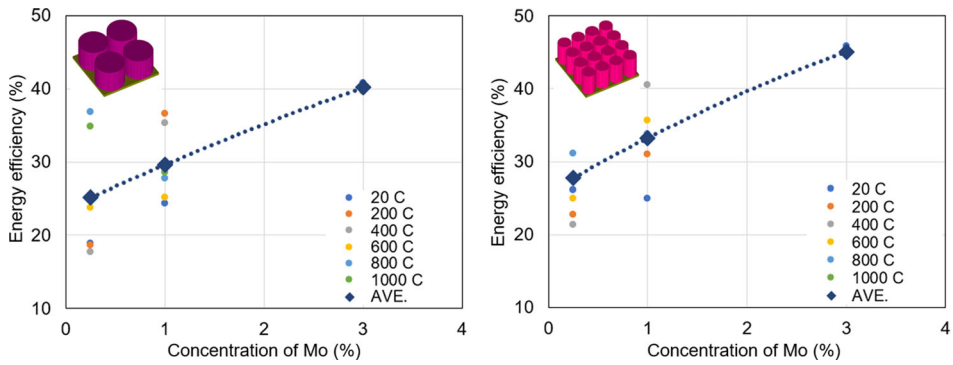
**Figure 14.** Energy efficiency (at different temperatures of the AlN:Mo composite and average) of the four- (a) and sixteen-cylinder systems (b) as functions of contents of Mo; off-normal incidence: $\theta = 10°$.
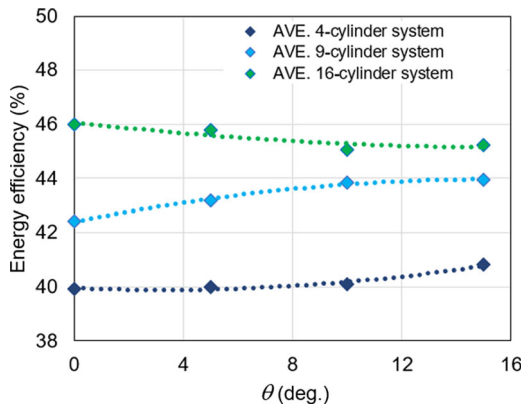
Figure 15. Energy efficiency (average for different temperatures of the AlN:Mo composite) of three systems with cylindrical susceptors as function of angel of deviation θ for Mo $= 3\%$.
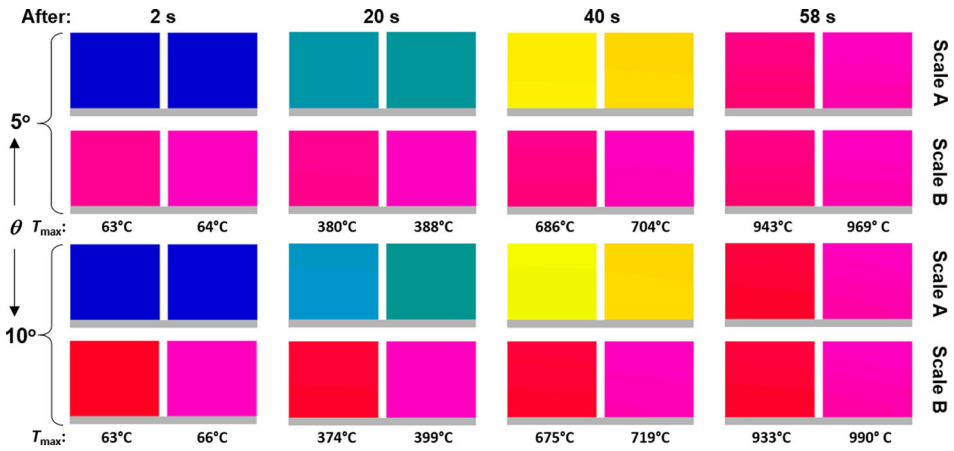
Figure 16. Time evolution of the temperature field in the vertical (xz -) plane through the two edge susceptors with Mo = 3.0% in the four-cylinder model; maximum values of temperature are included in each pattern; patterns are normalized to both Scale A and Scale B; heating time step in simulation is 2 s; incoming power density 430 W/mm^2; angles of deviation θ is 5° and 10°.
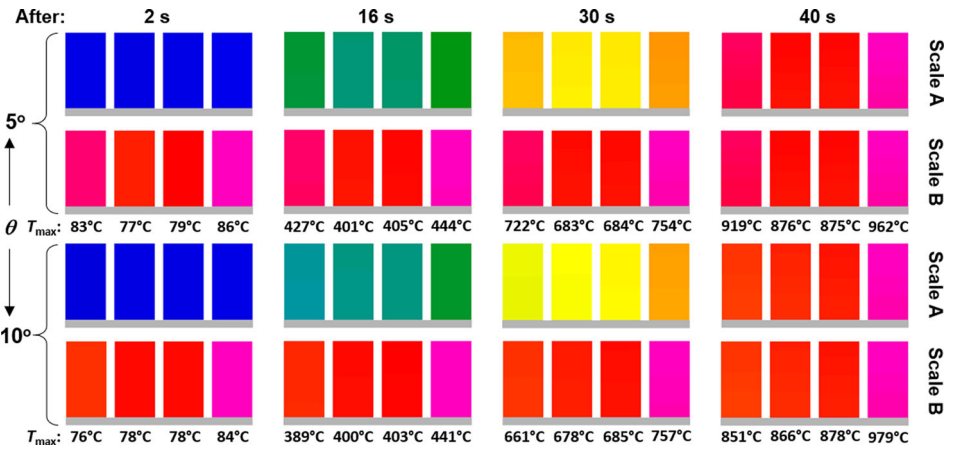
Figure 17. Time evolution of the temperature field in the vertical (xz -) plane through the four edge susceptors with Mo = 3.0% in the sixteen-cylinder model; maximum values of temperature are included in each pattern; patterns are normalized to both Scale A and Scale B; heating time step in simulation is 2 s; incoming power density 357 W/mm^2; angles of deviation θ is 5° and 10°.

from a normal incidence by 5 and 10°. It is seen that high uniformity of temperature distribution is maintained within each individual cylinder – apparently due to a high thermal conductivity of the AlN:Mo composite that supports quick spread of heat throughout the cylinders. At the same time, the difference between temperatures of different cylinders is now more significant, and this difference is larger for higher n (e.g. up to 120 °C in the sixteen-cylinder layout). Cylinders on the right of the rows are seen as gained the highest temperatures – apparently because the surfaces on their right sides are exposed to the incoming field with no shadow.

4. Discussion and conclusion

First, of note is the material at which energy efficiency of all the considered systems peaks. In all analyzed scenarios, the values of η is at its maximum when concentration of Mo in the composite is at the level of 3.0–4.0% Mo by volume. As the layouts with four, nine, and sixteen cylinders were introduced due to their high densities in the circles in a square packing problem, the densities calculated with consideration of the 1 mm gap between the cylinders turned out to be 0.722, 0.662, and 0.605, respectively. For the first two systems, the density is slightly higher than in the five-cylinder case ($d = 0.6$), but energy efficiency of all these alternative layouts appears to be of about the same level. Compared to the case of a single cubic susceptor, energy efficiency of all systems with multiple cylindrical absorbers is lower (for Mo = 3%, down to 37–45% from 50 to 55%) because the incoming plane wave now faces a portion of the reflecting metal baseplate.

When comparing the systems with cylindrical susceptors to one another, all models show very high levels of uniformity of temperature distribution within individual cylinders regardless the contents of Mo (0.25 to 4%). However, temperatures of different cylinders are not the same: the higher n, the larger that difference; e.g. it is up to 40 °C in the nine-cylinder system.

Off normal incidence of the plane wave does not make a notable impact on energy efficiency of the systems with cylindrical absorbers, at least, when the angle of deviation is less than $15°$. The oblique incidence, however, leads to the increase of the difference between maximum temperatures of the individual cylinders. For example, when $\theta = 10°$, in the sixteen-cylinder system made of the composite with Mo = 3% it may exceed, on the level of 1,000 °C, the level of 100 °C.

Overall, the output of the computational study presented in this paper provides support of the system design aiming to easy experimental development of the MMW HX with AlN:Mo susceptors. Prior characterization of functionality of prospective experimental systems through detailed modelling helps the designers narrow down with the choice from a wide range of conflicting options and come up with physical prototypes ready for efficient experimental development and tuning.

Disclosure statement

No potential conflict of interest was reported by the authors.

Notes on contributors

Catherine Hogan received her BSc degrees in physics and mathematical sciences from Worcester Polytechnic Institute, Worcester, MA, USA in 2021. During her undergraduate studies, she completed research in multiphysics modeling, millimeter wave technology, and power beaming applications. Her current research interests include space exploration through the astrophysics and space science fields. She is currently a Systems Engineer at the MIT RE Corporation, Bedford, MA, USA.

Brad Hoff is a Senior Scientist at the Air Force Research Laboratory working in the area of high power electromagnetics. He obtained a PhD from the University of Michigan (Ann Arbor, MI, USA) in 2009.

Ian M. Rittersdorf received the BSE, MSE, and PhD degrees in nuclear engineering and radiological sciences from the University of Michigan, Ann Arbor, MI, in 2008, 2010, and 2014, respectively. From 2014 to 2016 he was a National Research Council Post-Doctoral Fellow with the Naval Research Laboratory, Washington, DC, working with the Pulsed Power Physics Branch, Plasma Physics Division. His current research focus is on the development of numerical models for the evolution of electrode plasmas, high power microwaves, and the physics of high-power charged particle beam diodes for various applications.

Vadim Yakovlev is an Associate Research Professor in the Department of Mathematical Sciences, Worcester Polytechnic Institute, Worcester, MA, USA. He is a head of the Industrial Microwave Modeling Group which he formed in 1999 as a division of the WP I's Center for Industrial Mathematics and Statistics. He received his PhD degree in Radio Physics from the Institute of Radio Engineering and Electronics of the Russian Academy of Sciences, Moscow, Russia in 1991. His research interests include multiphysics modeling, microwave power engineering, microwave imaging, and power beaming applications.

ORCID

Brad W. Hoff http://orcid.org/0000-0002-6069-0395
Ian M. Rittersdorf http://orcid.org/0000-0003-4878-4230
Vadim V. Yakovlev http://orcid.org/0000-0001-7344-505X

References

Benford JN. 2008. Space applications of high-power microwaves. IEEE Trans Plasma Sci. 36(3):569–581.

Boll DW, Donovan J, Graham RL, Lubachevsky BD. 2000. Improving dense packings of equal disks in a square. Electron J Combin. 7(1):1–9.

Brown WC, Eves EE. 1992. Beamed microwave power transmission and its application to space. IEEE Trans Microwave Theory Techn. 40(6):1239–1250.

Celuch M, Kopyt P. 2009. Modeling of microwave heating of foods. In Lorence MW and Pesheck PS (Eds), Development of packaging and products for use in microwave ovens, Cambridge (UK): Woodhead Publishing, p. 305–348.

COMSOL Multiphysics. 1998–2020. COMSOL AB, www.comsol.com.

Coopersmith JC, Davis E. 2016. A strategic roadmap for commercializing low-cost beamed energy propulsion launch systems, Proc. AIAA SPACE, Art. no. 5555.

Gaone JM, Tilley BS, Yakovlev VV. 2019. Electromagnetic heating control via high-frequency resonance of a triple-layer laminate. J Eng Math. 114(1):65–86.

Goldberg M. 1970. The packing of equal circles in a square. Math Magazine. 43(1):24–30.

Hilario MS, Hoff BW, Jawdat BI, Dynys FW, Wang JJ. 2017. High temperature millimetre-wave permittivity measurement setup for beamed energy heat exchangers. 55th AIAA Aerospace Sciences Meeting, 2017,

Hilario MS, Hoff BW, Jawdat BI, Lanagan MT, Cohick AW, Dynys FW, Mackey JA, Gaone JM. 2019. W-band complex permittivity measurements at high temperature using free-space methods. IEEE Trans Compon Packag Manufact Technol. 9(6):1011–1019.

Hoff BW, Hilario MS, Jawdat BI, Baros AE, Dynys FW, Mackey JA, Yakovlev VV, Andraka CE, Armijo KM, Savrun E, Rittersdorf IM. 2018. Millimeter wave interactions with high temperature materials and their applications to power beaming, Proc. 52nd IMPI's Microwave Power Symposium, Long Beach (CA), 2018, p. 82–83.

Hoff BW, Dynys FW, Hayden SC, Grudt RO, Hilario MS, Baros AE, Ostraat ML. 2019a. Characterization of AlN-based ceramic composites for use as millimetre wave susceptor materials at high temperature: high temperature thermal properties of AlN:Mo with 0.25% to 4.0% Mo by volume. MRS Adv. 4(27):1531–1512.

Hoff BW, Hayden SC, Hilario MS, Grudt RO, Dynys FW, Baros AE, Rittersdorf IM, Ostraat MW. 2019b. Characterization of AlN-based ceramic composites for use as millimetre-wave susceptor materials at high temperature: dielectric properties of AlN:Mo with 0.25 v% to 4.0 v% Mo at temperatures from 25-550 °C. J Mater Res. 34(15):2573–2581.

Jamar A, Majid Z, Azmi W, Norhafana M, Razak A. 2016. A review of water heating system for solar energy applications. Int. Commun. Heat Mass Transfer. 76:178–187.

Jamnejad V, Silva A. 2008. Microwave power beaming strategies for fractionated spacecraft systems. Proc. 2008 IEEE Aerospace Conference, Big Sky, MT, March 2008, 14 pp.

Jawdat BI, Hoff BW, Hilario MS, Baros AE, Pelletier P, Sabo T, Dynys FW. 2017. Composite ceramics for power beaming. Proc. 2017 IEEE Wireless Power Transfer Conf., 978-1-5090-4595-3/17.

Koert P, Cha JT. 1992. Millimeter wave technology for space power beaming. IEEE Trans Microwave Theory Techn. 40(6):1251–1258.

Kopyt P, Celuch M. 2007. Coupled electromagnetic-thermodynamic simulations of microwave heating problems using the FDTD algorithm. J Microw Power Electromagn Energy. 41(4):18–29.

Koutchma T, Yakovlev VV. 2010. Computer modelling of microwave heating processes for food preservation. In: Farid M, editor, Mathematical analysis of food processing, CRC Press, Boca Raton (FL), p. 625–657.

Kumi P, Venne JS, Yakovlev VV, Hilario MS, Hoff BW, Rittersdorf IM. 2020a. Computational characterization of a composite ceramic block for a millimetre wave heat exchanger. In: Nicosia G and Romano V, editors, Scientific computing in electrical engineering, Cham: Springer, p. 65–74.

Kumi P, Martin SA, Yakovlev VV, Hilario MS, Hoff BW, Rittersdorf IM. 2020b. Electromagnetic-thermal model of a millimetre-wave heat exchanger based on an AlN:Mo susceptor. COMPEL. 39(2):481–496.

Landis GA. 1999. Beamed energy propulsion for practical interstellar flight. J. Brit. Interplanet Soc. 52:420–423.

Maranas CD, Floudas CA, Pardalos PM. 1995. New results in the packing of equal circles in a square. Discrete Math. 142(1-3):287–293.

Mohekar AA, Gaone JM, Tilley BS, Yakovlev VV. 2018. A 2D coupled electromagnetic, thermal and fluid flow model: Application to layered microwave heat exchangers. Proc. IEEE MTT-S Intern. Microwave Symp., Philadelphia (PA), 2018, p. 1389–1392.

Mohekar AA, Tilley BS, Yakovlev VV. 2019a. A 2D model of a triple layer electromagnetic heat exchanger with porous media flow. Proc. IEEE MTT-S Intern. Microwave Symp., Boston (MA), 2019, p. 59–62.

Mohekar AA, Tilley BS, Yakovlev VV. 2019b. Plane wave irradiation of a layered system: Resonance-based control over thermal runaway. Proc. 17th Intern. Conf. on Microwave and High Freq. Heating, Valencia (Spain), 2019, p. 292–300.

Mohekar AA, Tilley BS, Yakovlev VV. 2020. A triple layer electromagnetic heat exchanger with plane Poiseuille flow: control and local onset of thermal runaway. IEEE J Multiscale Multiphys Comput Tech. 5:119–131.

Parkin KL, DiDomenico LD, Culick FE. 2004. The microwave thermal thruster concept. Proc. 2nd Intern. Symp. Beamed Energy Propulsion, 2004, p. 418–429.

Rittersdorf IM, Hoff BW, Richardson AS, Martin SA, Yakovlev VV, Kim PS, Schumer JW. 2021. A one-dimensional model for the millimetre-wave absorption and heating of dielectric materials in power beaming applications. IEEE Trans Plasma Sci. 49(2):695–702.

Rodenbeck CT, Jaffe PI, Strassner BH, Hausgen PE, McSpadden JO, Kazemi H, Shinohara N, Tierney BB, DePuma CB, Self AP. 2021. Microwave and millimetre wave power beaming. IEEE J Microw. 1(1):229–259.

QuickWave. 1998–2021. QWED Sp. z o. o., www.qwed.eu.

Sayigh A. 2012. Comprehensive renewable energy, Amsterdam: Elsevier.

Sienna Technologies. 2011. http://siennatech.com/wp-content/uploads/2011/10/ST-200-AIN-Thermal-Conductivity.pdf.

Yakovlev VV, Allan SM, Fall ML, Shulman HS. 2011. Computational study of thermal runaway in microwave processing of zirconia. In Tao J, editor, Microwave and RF power applications, Cépaduès Éditions, Toulouse, p. 303–306.